PNAS

www.pnas.org

Supplementary Information for
A dynamical model for generating synthetic data to quantify active tactile sensing behavior in the rat.

Nadina O. Zweifel[1], Nicholas E. Bush[2], Ian Abraham[3], Todd D. Murphey[3], Mitra J.Z. Hartmann[1,3]

[1] Department of Biomedical Engineering, Northwestern University, Evanston, Illinois, 60208
[2] Interdepartmental Neuroscience Program, Northwestern University, Evanston, Illinois, 60208
[3] Department of Mechanical Engineering, Northwestern University, Evanston, Illinois, 60208

Corresponding Author:
Mitra J.Z. Hartmann
hartmann@northwestern.edu

This PDF file includes:

Other supplementary materials for this manuscript include the following:

S.1. Model of a single whisker

The model of a single whisker was created using the Bullet Physics Library (1) and extends a previous two-dimensional (2D) model (2) to three dimensions (3D). The whisker is modeled as a chain of N conical frustums (links) connected by N-1 equidistant joints (nodes). The length of the links $l_{link} = S/N$ depends on the whisker arclength S and the number of links N, while the radius at each node r_n decreases linearly from the whisker base to the tip (eq. S1). Schematics of two views of the model are shown in Figure S1.

$$r_n = r_{base} - \left(\frac{n-1}{N}\right)(r_{base} - r_{tip}), \text{where } n = 1, ..., N+1 \hspace{2cm} \text{(eq. S1)}$$

Each link has mass $m_n = \rho_n \frac{\pi\, l_{link}}{3}(r_n^2 + r_n r_{n+1} + r_{n+1}^2)$, where density $\rho_n = \rho_{base} - \left(\frac{n-1}{N}\right)(\rho_{base} - \rho_{tip})$ increases linearly from base to tip. Values for density at the base (ρ_{base}) and the tip (ρ_{tip}) were obtained from a previous study (3).

Nodes 2 through N are modeled as torsional spring-dampers with two degrees of freedom, permitting rotations about the y and z axes. The parameters k_n and c_n represent stiffness of the spring and damping in the two bending directions (rotations about the y and z axes). Twist of the whisker (rotation about the x-axis) was omitted. The whisker follicle is represented by node 1. The follicle is pinned (cannot translate) and its rotation about all three axes is rigidly controlled. As described in section S.3.2, a torsional spring-damper was later added to model the tissue elasticity of the follicle in the skin, allowing rotations about the y and z axes.

Theoretically, each node can be viewed as the pivot point of a pendulum (2). The adjacent distal portion of the whisker has mass M_n, which determines the mass of the pendulum, and the distance $L_{com,n}$ between its center of mass (com) and the nth node determines the length of the pendulum. Thus, the stiffness and damping of the spring associated with the node can be calculated as:

$$k_n = \frac{E_n I_n}{l_{link}} \hspace{4cm} \text{(eq. S2)}$$

$$c_n = 2\zeta_n L_{com,n}\sqrt{M_n k_n} \hspace{3cm} \text{(eq. S3)}$$

where E_n is Youngs's modulus and I_n is the area moment of inertia of the associated link. The variable ζ_n represents the damping ratio of the spring of the nth node.

From equations S2 and S3 and $I_n = \frac{\pi r_n^4}{4}$, it is clear that the stiffness and damping at each node are primarily determined by the geometry of the whisker. Following the methods of previous studies (2, 4-10), our model assumes uniform Young's modulus and uniform damping ratio, i.e., $E_0 = E_1 = \cdots = E_n$ and $\zeta_0 = \zeta_1 = \cdots = \zeta_n$. We denote the corresponding model parameters as θ_E and θ_ζ. We optimized parameters θ_E and θ_ζ using kinematic data obtained from a real whisker.

S.2. Experiments for model optimization

To optimize and validate the model we performed two separate experiments. The first experiment (Experiment 1) involved rotating whiskers on a motor in the horizontal plane, resulting in motion that was approximately 2D although 3D motion was quantified. Data from this first experiment were used to optimize material parameters (Young's modulus and damping coefficient) for the model. The second experiment involved manual deflections of different whiskers in the anesthetized animal. The whiskers were deflected in several different directions, and these data were used to optimize the constants of the spring modeling the elasticity of the follicle.

The first experiment used two whiskers, α and B1, whose geometric parameters are listed in Table S1. Both whiskers were trimmed so that their tips could be clearly seen in the video, therefore they both have a shorter arc length and larger tip diameter than typical. The base of each whisker was fixed to the vertical shaft of a DC motor and rotated in a "gaussian pulse" motion. The whisker was oriented so that its intrinsic curvature coincided approximately with the horizontal plane. The motor was controlled using a microcontroller (PIC32) running a feedback controller at 5 kHz. At the beginning of each trial, the initial motor position was set to 0° and the microcontroller was synchronized with two orthogonally-mounted high-speed video cameras (Mikrotron 4CXP; E1: 1000fps; E2: 500 fps, later upsampled to 1000 fps) used to track the whisker's motion. The amplitude, speed and frequency of the driving signal was varied (Table S1) and each parameter combination was repeated five times. After data collection, the whisker was removed from the motor and the base diameter (at the fixation point on the motor) and length were measured using a microscope (Leica DM750).

The second set of experiments (Experiment 2) was performed in the anesthetized rat as part of a separate study (11). All whiskers except for one were trimmed down to the length of the fur. The spared whisker was manually deflected with a graphite probe in eight cardinal directions, at two or three different contact points along its length, at two different speeds. Five different whisker identities from 11 different animals were used.

In both Experiments 1 and 2, the 3D whisker reconstruction from the two orthogonal camera views was performed in three steps. First, the whiskers were tracked in 2D using the software "Whisk" (12). In each view, the 2D tracked whisker shapes were cleaned and smoothed. Second, the two cameras were calibrated with the Caltech Camera Calibration Toolbox, OpenCV, and custom Matlab and python code. Finally, an iterative optimization was used to find the best 3D whisker shape that minimized the 2D back-projection error, defined as the Euclidean distance between the back-projected whisker and the actual, imaged whisker, summed over all back-projected points.

To analyze the manual deflections in Experiment 2, we used semi-automated tracking code to determine the 3D contact point and time at which the graphite probe made contact with the whisker. The 3D tracking data was filtered with a thresholded median (Hampel) filter using a window size of 3 frames and a threshold of 1.5 standard deviations for outliers.

Finally, the best trials were manually selected for each whisker in both experiments. The resulting datasets are shown in Table S2.

S.3. Model optimization
Two optimizations were performed to match the simulated dynamics with the dynamics of real whiskers. The first optimization determined optimal values of the model parameters of the single whisker model (θ_E and θ_ζ) using data collected *ex vivo* (Experiment 1), while the second optimization was used to find the optimal values for the follicle parameters (stiffness and damping) using data collected *in vivo* (Experiment 2).

S.3.1. Optimization of single-whisker dynamics in two dimensions
In order to optimize the parameters θ_E and θ_ζ, the motor setup described for Experiment 1 was replicated in simulation using Bullet Physics Library (1, 13).

Because whisker dynamics depended on the geometry of the whisker, the single whisker model was modified to accurately match the dimensions and shape of the real whisker in the experiment (Table S1). The 3D data points of the first frame were used to reconstruct the whisker in simulation. These data points defined the locations of the nodes and the length of the links between them, respectively. The smoothed driving signal of the motor was used to control the angular displacement of the whisker base about the axis of rotation.

The mechanical signals at the whisker base are primarily determined by its geometry and its material properties, stiffness and damping. In the single-whisker model, stiffness and damping of the whisker are set by stiffness and

damping at each node, which are a function of Young's modulus (E) and damping ratio (ζ), respectively (eq. S2 and S3). The true values of E and ζ are unknown and therefore constitute the free parameters of our model, denoted as θ_E and θ_ζ. We assume that θ_E and θ_ζ are constant and the same for all nodes and all whiskers, so they only approximate E and ζ, respectively. The parameters θ_E and θ_ζ were optimized using experimental data from two large, caudal rat whiskers, obtained from array positions α and B1. Each whisker was attached to a motor and driven with a Gaussian pulse at three different speeds, which allowed us to quantify the dynamic behavior of the whisker based on the resonance frequency (f_n) and logarithmic decrement (δ) of the induced oscillations.

The experiment was then replicated in simulation using the single-whisker model with the known arc length, curvature, and base diameter of the real whiskers. To avoid local minima, we used a brute-force approach to iterate through 1296 combinations of θ_E and θ_ζ values within a specific range (θ_E was varied between 2.0 and 6.5 GPa and θ_ζ between 0.15 and 0.6). For each pair of parameter values, five trials were randomly sampled for each of the two whiskers. Then each trial was simulated and evaluated in terms of its first-mode resonant frequency (FRF), logarithmic decrement δ, and peak amplitude A, computed from the y trajectory of the whisker tip evolving over 1000 samples (= 1 second). The FRF was determined by finding the peak of the power spectrum computed via the Fast Fourier Transform (FFT). The value of δ was calculated in the time domain. Given the magnitudes of the first two adjacent peaks, y_0 and y_1, $\delta = \ln\left(\frac{y_0}{y_1}\right)$. The value of y_0 was used as measurement for peak amplitude A.

We used the median symmetric accuracy (MSA) (14) to quantify the total error of the simulations across the 10 trials. The MSA was computed using eq. S4a, where simulated and experimental measurements are denoted by the subscript sim and exp, respectively. The median was calculated from the pooled FRF, δ, and A measurements across all 10 trials.

$$MSA\left(\theta_E, \theta_\zeta\right) = exp\left\{median\left(\left|\ln\left(\frac{FRF_{sim}(\theta_E,\theta_\zeta)}{FRF_{exp}(\theta_E,\theta_\zeta)}\right)\right|, \left|\ln\left(\frac{\delta_{sim}(\theta_E,\theta_\zeta)}{\delta_{exp}(\theta_E,\theta_\zeta)}\right)\right|, \left|\ln\left(\frac{A_{sim}(\theta_E,\theta_\zeta)}{A_{exp}(\theta_E,\theta_\zeta)}\right)\right|\right)\right\} - 1 \qquad \text{(eq. S4a)}$$

The optimal parameter values θ_E^* and θ_ζ^* were obtained by finding the parameter combination yielding the minimum MSA across all parameter evaluation:

$$\theta_\zeta^*, \theta_E^* = \underset{\substack{\theta_E\in[2.0,6.5],\\ \theta_\zeta\in[0.15,0.6]}}{argmin}\ MSA\left(\theta_E, \theta_\zeta\right) \qquad \text{(eq. S5).}$$

As shown in Figure S2a, the minimum of the error surface was found to be located at θ_E = 5.0 GPa and θ_ζ = 0.33. Values of the true Young's modulus have been reported to fall between 1.3-7.8 GPa (4-6, 15, 16), while the true damping ratio has been estimated between 0.05 and 0.28 (4, 5, 10).

Given these optimized parameters, the actual dynamic properties measured from simulated trajectories were in good agreement with values observed experimentally (Table S3). Moreover, the resonance frequencies of 65 Hz and 59 Hz and damping ratio of 0.08 and 0.04 for the simulated α and B1 whisker, respectively, are well within observed biological variability. Whiskers with dimensions similar to the α whisker have first-mode resonance frequencies between 59 – 83 Hz; those with dimensions similar to B1, between 50 – 59 Hz (4, 5). The damping ratio calculated from the kinematic behavior of the whisker is smaller than the optimized value for parameter θ_ζ. This difference is likely attributable to the assumption that the damping ratio is uniform along the whisker, as previous studies have suggested that the damping ratio decreases from base to tip (4, 7, 10).

Matching material properties between simulation and experiment does not guarantee that simulated dynamics will accurately match experimental data. Nevertheless, simulated trajectories of the whisker tip closely followed experimentally obtained trajectories (Figure S2b). The high accuracy of the predictions is confirmed by a fit close

to the identity line in Figure S2c for the α whisker, with a slope of 1.1 for both x- and y- coordinates. Results for the B1 whisker were similar but had a slightly larger bias in the y direction, with a slope of 1.3. High Pearson correlation coefficients for both whiskers, α (x: 0.92, y: 0.92) and B1 (x: 0.99, y: 0.78) also indicate a close match between simulation and experiment for both whiskers. Note that the trajectory error shown in Figure S2b and Figure S2c are the largest observed, because the error increases with the distance to the actuation point, i.e., the whisker base (Figure S2d). The maximum error at the tip is 1.6 mm and decreases rapidly to less than 1 mm at 80% of the whisker length. At 50%, the error is already less than 0.3 mm and nearly zero (< 0.1 mm) at the base.

S.3.2. Optimization of damping properties of the follicle

The *ex vivo* model described above assumes that the whisker is rigidly anchored in the follicle (Figure S3a, rigid base). However, a preliminary analysis immediately indicated that simulations assuming a rigid follicle generated deflections that were nearly an order of magnitude larger than those observed in Experiment 2 (whisker deflections *in vivo*, in the anesthetized animal.). The discrepancy between rigid-base simulations and experimental results are clearly shown in (Figure S3b, top panel). In other words, the experimental trajectory of the whisker tip was considerably more damped than the dynamics of the rigidly anchored simulations.

We therefore aimed to incorporate elasticity at the whisker base, simulating the insertion of the whisker-follicle complex into compliant skin tissue (Figure S3a, compliant base). We added two identical torsional springs about the y and z axis of the base of the whisker to account for the compliant tissue properties of the follicle. In contrast to the single whisker model, the stiffness and damping parameters of the torsional spring-damper system in the follicle are not directly related to any specific material properties.

The spring stiffness and damping of these springs were then optimized using similar procedures as for the optimization of model parameters θ_E and θ_ζ. Randomly selected trials from the B1, B2, and D2 whiskers from Experiment 2 were used. Because the oscillations of the whiskers in Experiment 2 were very small, the logarithmic decrement δ was difficult to measure. The error metric in eq. S4a was therefore adjusted to include only the error in FRF and the error in the magnitude of the first two adjacent peaks y_0 and y_1 of the whisker tip oscillations (eq. S4b).

$$MSA(\theta_E, \theta_\zeta) = exp\left\{median\left(\left|\ln\left(\frac{FRF_{sim}(\theta_E,\theta_\zeta)}{FRF_{exp}(\theta_E,\theta_\zeta)}\right)\right|, \left|\ln\left(\frac{y_{0,sim}(\theta_E,\theta_\zeta)}{y_{0,exp}(\theta_E,\theta_\zeta)}\right)\right|, \left|\ln\left(\frac{y_{1,sim}(\theta_E,\theta_\zeta)}{y_{1,exp}(\theta_E,\theta_\zeta)}\right)\right|\right)\right\} - 1 \qquad \text{(eq. S4b)}$$

For each parameter combination, three trials were randomly sampled for each whisker and the MSA computed according to eq. S4b. Again, the optimal values were determined by finding the minimum error across all simulated parameter combinations.

After optimization, the trajectory of the whisker much more closely resembled the experimental data (Figure S3b, bottom panel). In addition, as shown in Figure S3c, the Pearson correlation coefficients between experiment and simulation for both horizontal and vertical deflections for each whisker achieve an average R value of 0.63 (±0.15). These results indicate that the model can robustly predict dynamics at the whisker base even after accounting for the compliant properties of the follicle embedded within the tissue

As expected, the difference between rigid and compliant follicle is also evident in the mechanical signals predicted to occur at the whisker base. Figure S3d shows an example of the forces in bending direction (F_z) and moment about the axis of rotation (M_y) for a B1 whisker corresponding to the tip trajectory in Figure S3b. Compared to the rigid follicle model, the compliant follicle model reduces F_z and M_y by more than an order of magnitude while it also exhibits low pass properties smoothing the mechanical response (bottom plots).
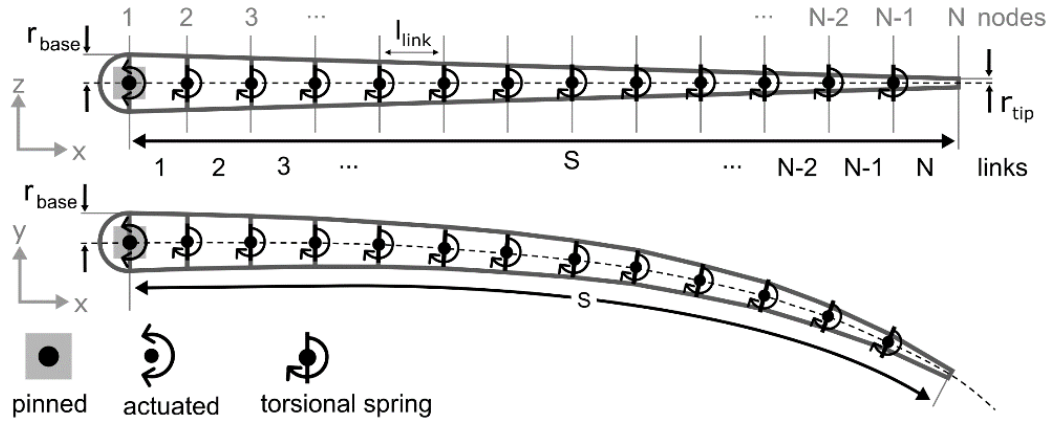
Figure S1. Schematics illustrate the whisker model used in all simulations. The whisker is rigidly driven from node 1, which represents the follicle. The node is pinned so that it can rotate but not translate. Nodes 2-N each represent a 3D torsional spring damper. The whisker is straight in the x-z plane and has intrinsic curvature in the x-y plane. In each simulation the curvature was chosen to be appropriate for the specific whisker being simulated (see text for details). For the optimization of spring stiffness and damping parameters of nodes 2-N, the geometry of the whisker (arc length S, base radius r_{base} and tip radius r_{tip}) were obtained from the real whiskers used in the experiments.
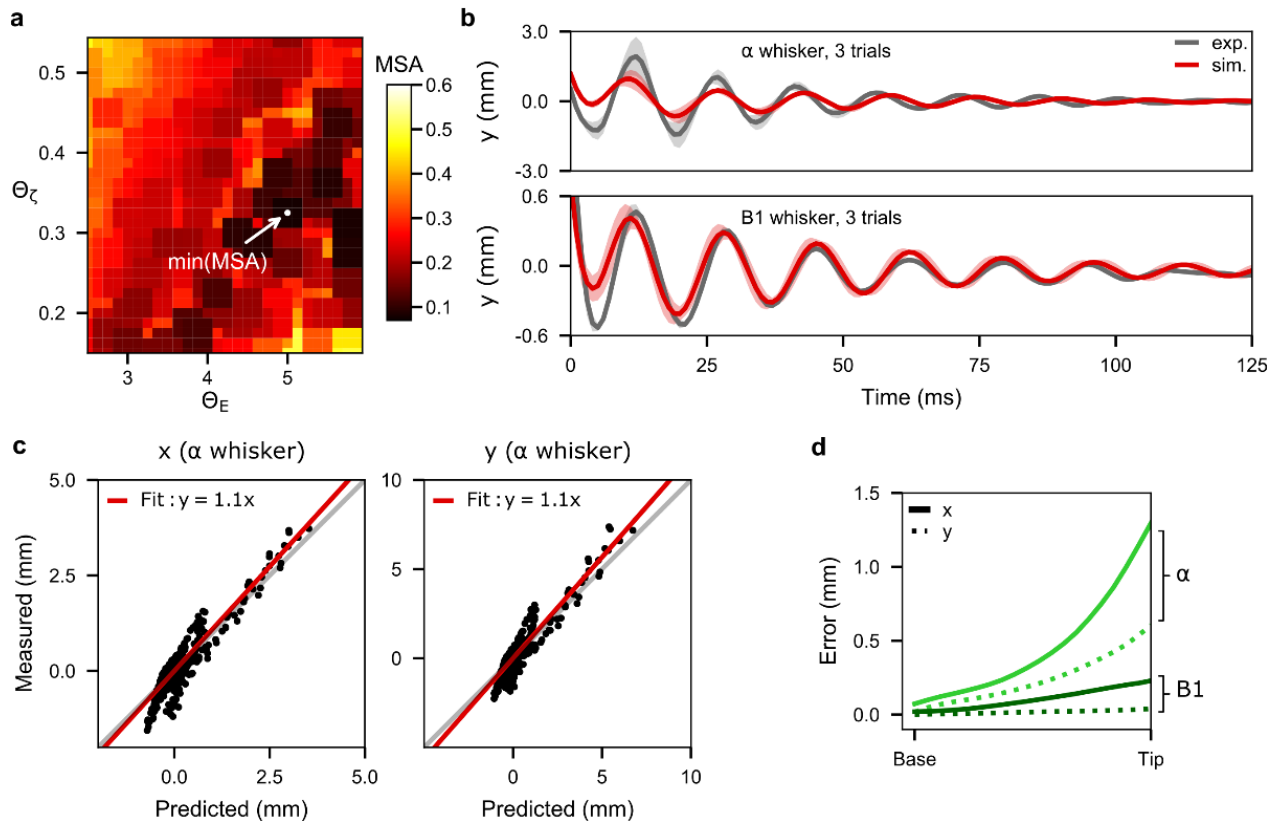
Figure S2. Parameter optimization with a single whisker yields good match with experimental data. (a) Error surface generated by optimizing the parameters θ_ζ and θ_E. Color represents error between simulated and experimental data. Note the linear relationship between θ_E and θ_ζ, reflecting the tradeoff between fitting the resonance frequency and fitting the log-decrement. **(b)** Averaged trajectory of the whisker tip in the y-direction for three trials in which the α and B1 whiskers were driven at the same speed in experiment and simulation. The variability indicated by the standard deviation across the trials occurs because the motor angle is non-deterministic. **(c)** Measured versus predicted trajectory (x- and y- coordinates) of the α whisker tip in the horizontal plane over all trials used for the optimization. **(d)** Displacement error increases as a function of link position (distance from whisker base). Note that the error of the tip, which was used for optimization, is largest; error decreases rapidly to less than 0.3 mm at 50% of the whisker length. Data are shown for the α (green) and B1 (black) whiskers; x- and y- coordinates are shown as dashed and solid lines, respectively.
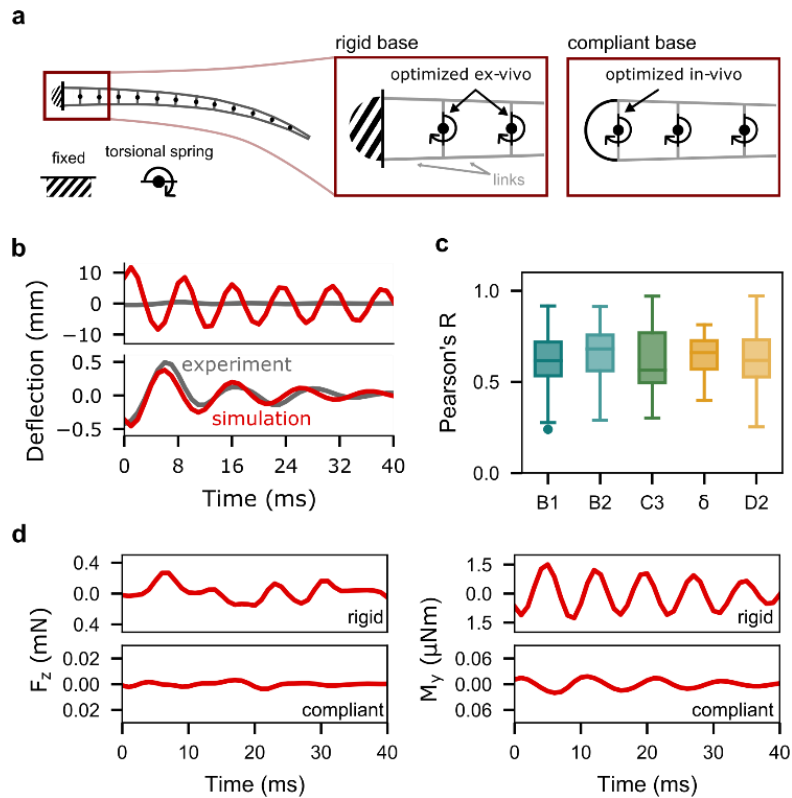
Figure S3. Mechanical properties of the follicle significantly affect whisker dynamics and mechanical signals at the whisker base. **(a)** Schematic of the single-whisker model and the constraints used for the rigid base (fixed) and the compliant base (torsional spring). The red square marks the magnified part to the right. A whisker attached to a motor was used to optimize the torsional springs connecting the individual links of the whisker body while the base was fixed (middle). In a second step the fixed constraint at the base was replaced with a torsional spring that was optimized using deflection data from an in-vivo experiment (right). **(b)** Displacement of the whisker tip of a representative trial in which the B1 whisker was deflected. The grey traces in both panels show the oscillations measured experimentally, which include the compliant properties of the follicle. The red traces show simulation results when assuming a rigid follicle condition for experiment (upper panel) and after incorporating the compliant properties of the follicle (lower panel). **(c)** Pearson correlation between experimental and simulated trajectory of the most distal link for five different whiskers, labeled on the x-axis, pooled over horizontal and vertical directions. Distributions were computed across all trials for each whisker. R = 0.61 (±0.14) for B1 whisker, R = 0.66 (±0.15) for B2 whisker, R = 0.61 (±0.19) for C3, R = 0.63 (±0.12) for D0 whisker, and R = 0.61 (±0.12) for D2 whisker. **(d)** Force in bending direction, F_z (left), and moment about the bending axis, M_y (right) in rigid (upper panel) and compliant (lower panel) follicle condition.
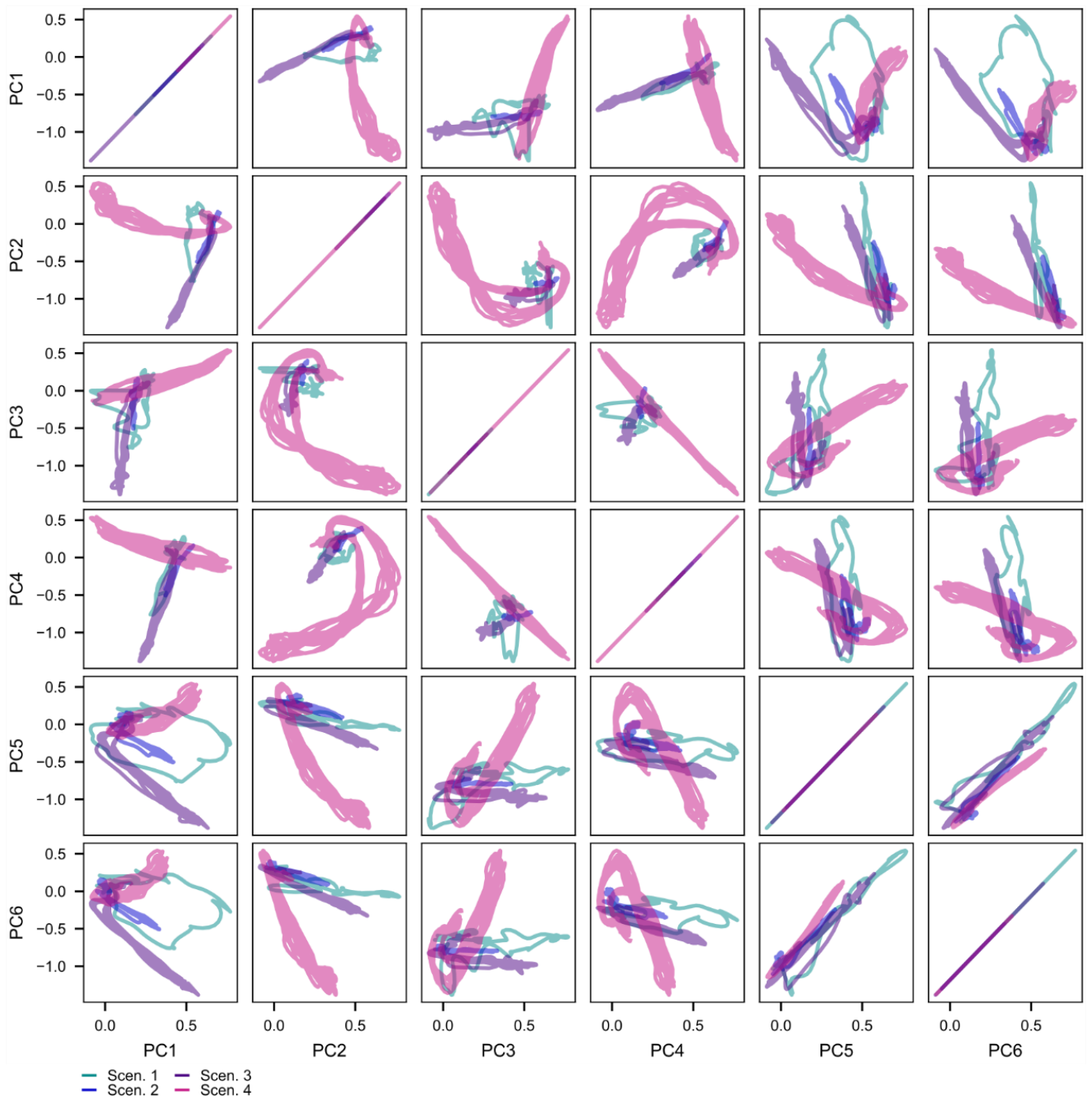
Figure S4. Mechanosensory signals in the principal component (PC) space. The mechanosensory signals were projected onto pairs of the six leading PCs for each of the four scenarios. The four trajectories separate the best when projected onto PC1 and PC5, while the trajectories of Scenario 3 and 4 are most separated in the PC1 and PC2 plane.
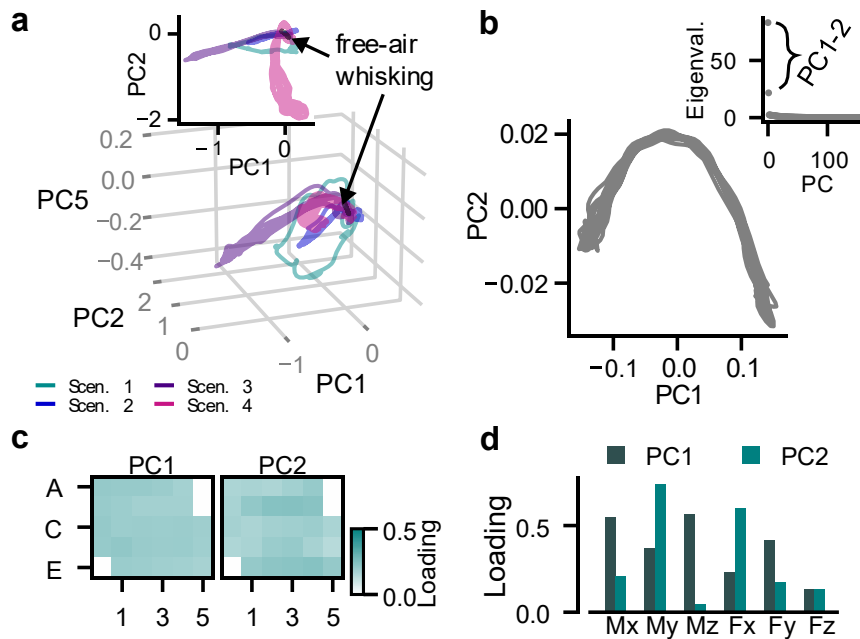
Figure S5. Principal Component Analysis for the mechanical signals generated during non-contact whisking. (a) Projection of the 162-dimensional signal space (6 mechanical components * 27 whiskers) onto the principal components PC1, PC2, and PC5 for each of the scenarios shown in Figure 4d in the main text. Color code matches that of Figure 4d. *Inset*: projection of the mechanosensory signals into the PC1-PC2 plane. The projections for non-contact whisking are shown in black as indicated by the arrows. The mechanical signals generated during non-contact whisking stem from the inertial effects of the whiskers and thus are very small in magnitude. **(b)** The mechanical signals projected onto the first two leading PCs as estimated by the data simulated during non-contact whisking, without collision (Scen. 1-4). The periodic nature of the signals stems from the repetitive whisking motion, which changes the orientation of the whiskers and thus the inertial effects throughout the whisking cycle. *Inset*: eigenvalues of the principal components (PCs). **(c)** Total loadings of each whisker for the two leading PCs corresponding to (b), obtained by summing over all 6 mechanical components. In contrast to the four collision scenarios in Figure 4e, all whiskers contribute almost equally to the PCs. **(d)** Total loadings for each of the mechanical components for the two leading PCs corresponding to (b), obtained by summing over all whiskers. The loads of the first PC indicate highest contribution from the components M_x, M_z, and F_y. This result makes sense because the largest change occurs in the horizontal plane, which affects M_z and F_y the most. In contrast, M_x responds to torsion and the combination of elevation and protraction of the whisker.

Table S1. Dimensions of the whiskers and motor parameters used in Experiment 1

Dimensions of the whiskers			
Whisker	**Arc length (mm)**	**Base diameter (µm)**	**Tip diameter (µm)**
α	29.6	120	35
B1	34.1	131	30

Motor parameters		
Parameter	**Variable**	**Values**
Driving signal	N/A	$\varphi(A, \omega) = Ae^{-\omega(t-t_0)^2}$
Amplitude (deg)	A	45
Speed (deg/s)	ω	900, 2000, 3500
Frequency (Hz)	f	-
Time offset (s)	t_0	45/200

Table S2. Datasets for Experiment 1 and Experiment 2

	Whisker identities	**Number of trials**
Experiment 1	α	10
	B1	6
Experiment 2	B1	83
	B2	63
	C3	13
	D0	28
	D2	74

Table S3. Dynamic measurements of experiment and optimized simulation.

Variable and units	**whisker**	**Experiment**	**Simulation**	**Absolute Error**
f_n (Hz)	α	67.6 (±0.72)	64.87 (±1.12)	2.73 (±1.28)
	B1	59.38 (±0.44)	58.96 (±0.68)	0.86 (±0.61)
δ (dimensionless)	α	0.32 (±0.23)	0.50 (±0.4)	0.26 (±0.37)
	B1	0.25 (±0.08)	0.23 (±0.08)	0.04 (±0.06)
ζ (dimensionless)	α	0.05 (±0.04)	0.08 (±0.06)	0.04 (±0.06)
	B1	0.04 (±0.01)	0.04 (±0.01)	0.01 (±0.01)

Movie S1. Visualization of the passive stimulation experiment (Scenario 1). A vertical peg was simulated to move from rostral to caudal through the middle of the immobile right array. The peg moves at constant speed (0.3 m/s) from rostral to caudal. The right upper panel shows the visualization of the 3D simulation, showing the rat head and the right whisker array. The upper left quadrant shows two illustrations of the mystacial pad, each circle representing a follicle. The color scale on the left indicates the magnitude of the of the bending moment M_b ($= \sqrt{M_y^2 + M_z^2}$) whereas the color scale on the right indicates the magnitude of the transverse force F_t ($= \sqrt{F_y^2 + F_z^2}$) generated at the base of each whisker. Underneath, the whisker basepoints are plotted in 3D (white dots), while the 3D vectors of the mechanical signals are superimposed at each basepoint. Note that the view angle is different from the visualization. The bottom left panel shows M_b (same color scale) evolving over time for each of the whiskers (y-axis). Similarly, the bottom right panel, shows the point of contact for each whisker over time, indicated by the grey color scale. The point of contact is normalized to the length of the whisker, i.e. tip = 1.0.

Movie S2. Visualization of active whisking against two vertical pegs (Scenario 2). Same as in Movie S1, but instead of a single sweep through the entire array, the peg oscillates back and forth between its start and end position (in the middle of the array) to repeatedly stimulate the array eight times per second (8Hz). This scenario was carefully designed to replicate as closely as possible the stimulation distances, velocities, and frequencies associated with active whisking (Scenario 3).

Movie S3. Visualization of active whisking against two vertical pegs (Scenario 3). Simulation of active whisking against a fixed, vertical peg. Each whisker is driven at its base according to established kinematic equations for whisking motion (19). One cycle of protraction and retraction of the array lasts 125 ms, equivalent to a whisking frequency of 8 Hz. The peg is positioned laterally, 20 mm from the midline of the head with an offset of 10 mm from the nose tip.

Movie S4. Visualization of natural environment experiment (Scenario 4). Whiskers perform the identical whisking motion as in Movie S3 (Scenario 3), but the array is positioned in front of the opening of a 3D scan of a drainpipe, so that the rat is simulated to actively palpate a typical object found in its natural habitat.

Dataset S1 (separate file). Experimental data used in Figure 1 in the main text. The dataset consists of three different datasets compiled from the literature that include measurements of whisker resonances and whisker arc length. The first dataset is from Hartmann et al., 2003, including data of 24 whiskers from one rat (4). The second from Wolfe et al., (2008) consisting of 22 whiskers (δ, D1, D2, D3, D4) from four different rats (17). The third dataset is from Neimark et al. (2003) providing resonance frequencies of 10 whiskers of the C-row (left and right) measured both in vivo and ex vivo (5).

References

1.   E. Coumans (2015) Bullet Physics Simulation. in *ACM SIGGRAPH 2015 Courses* (ACM, New York, NY, USA).

2.   B. W. Quist, V. Seghete, L. A. Huet, T. D. Murphey, M. J. Hartmann, Modeling forces and moments at the base of a rat vibrissa during noncontact whisking and whisking against an object. *J Neurosci* **34**, 9828-9844 (2014).

3.   A. E. Yang, H. M. Belli, M. J. Z. Hartmann, Quantification of vibrissal mechanical properties across the rat mystacial pad. *J Neurophysiol* **121**, 1879-1895 (2019).

4.   M. J. Hartmann, N. J. Johnson, R. B. Towal, C. Assad, Mechanical Characteristics of Rat Vibrissae : Resonant Frequencies and Damping in Isolated Whiskers and in the Awake Behaving Animal. **23**, 6510-6519 (2003).

5.   M. A. Neimark, M. L. Andermann, J. J. Hopfield, C. I. Moore, Vibrissa resonance as a transduction mechanism for tactile encoding. *The Journal of neuroscience : the official journal of the Society for Neuroscience* **23**, 6499-6509 (2003).

6.   B. W. Quist, R. A. Faruqi, M. J. Z. Hartmann, Variation in Young's modulus along the length of a rat vibrissa. 10.1016/j.jbiomech.2011.08.027 (2011).

7.   Y. Boubenec, D. E. Shulz, G. Debrégeas, Whisker encoding of mechanical events during active tactile exploration. *Frontiers in Behavioral Neuroscience* **6**, 1-16 (2012).

8.   K. Carl *et al.*, Characterization of statical properties of rat's whisker system. *IEEE Sensors Journal* **12**, 340-349 (2012).

9.   W. Yan *et al.*, A truncated conical beam model for analysis of the vibration of rat whiskers. *Journal of Biomechanics* **46**, 1987-1995 (2013).

10.   R. Vaxenburg, I. Wyche, K. Svoboda, A. L. Efros, S. A. Hires, Dynamic cues for whisker-based object localization: An analytical solution to vibration during active whisker touch. *PLOS Computational Biology* **14**, e1006032-e1006032 (2018).

11.   N. E. Bush, S. A. Solla, M. J. Z. Hartmann, Continuous, multidimensional coding of 3D complex tactile stimuli by primary sensory neurons of the vibrissal system. *bioRxiv* (2019).

12.   N. G. Clack *et al.*, Automated tracking of whiskers in videos of head fixed rodents. *PLoS Comput Biol* **8**, e1002591 (2012).

13.   C. Erwin, J. McCutchan (2008) Bullet Physics Library.

14.   S. K. Morley, T. V. Brito, D. T. Welling, Measures of Model Performance Based On the Log Accuracy Ratio. *Space Weather* **16**, 69-88 (2018).

15.   Q. Kan, R. Rajan, J. Fu, G. Kang, W. Yan, Elastic modulus of rat whiskers—A key biomaterial in the rat whisker sensory system. *Materials Research Bulletin* **48**, 5026-5032 (2013).

16.   V. R. Adineh, B. Liu, R. Rajan, W. Yan, J. Fu, Multidimensional characterisation of biomechanical structures by combining Atomic Force Microscopy and Focused Ion Beam: A study of the rat whisker. *Acta Biomater* **21**, 132-141 (2015).

17.   J. Wolfe *et al.*, Texture coding in the rat whisker system: slip-stick versus differential resonance. *PLoS Biol* **6**, e215 (2008).